Journal of Materials Chemistry A

PAPER

View Article Online
View Journal | View Issue

Cite this: J. Mater. Chem. A, 2018, 6, 13331

A two-dimensional cationic covalent organic framework membrane for selective molecular sieving†

Wenxiang Zhang,[ab] Liming Zhang,[a] Haifeng Zhao,[a] Bin Li *[a] and Heping Ma *[c]

Received 5th May 2018
Accepted 11th June 2018

DOI: 10.1039/c8ta04178d

rsc.li/materials-a

The search of new-type membrane materials with ideal molecular sieving caused wide interest in both academia and industry. Covalent organic frameworks (COFs) are excellent candidates for efficient molecular separation because of their well-defined pore structure and fine-tuned pore size. However, existing synthetic approaches of COFs mainly result in an insoluble and unprocessable powder, which severely restricts their widespread applicability. In this work, a facile bottom-up interfacial crystallization approach to obtain a two-dimensional (2D) cationic COF, EB-COF:Br nanosheets, is reported. Then a layer-by-layer restacking process is performed to fabricate a continuous and dense 2D ionic COF membrane with a tunable thickness by simple vacuum filtration. The 2D COF membrane shows much higher solvent permeability than graphene-oxide membranes and commercial nanofiltration membranes because of its high porosity. Moreover, due to there being abundant positive charge sites in its pore walls, the EB-COF:Br membrane demonstrates highly selective sieving performance for dye molecules/ions with different charges and sizes. The EB-COF:Br membrane can efficiently reject ~>98% of anionic dye molecules/ions, while maintaining high solvent permeability. The cationic 2D COF membrane far outperforms other nanofiltration membranes in terms of excellent selective molecular/ionic sieving and superior solvent permeability. The result suggested that the ionic COF membrane can offer a new avenue for separation technology.

Introduction

Porous membranes with a controllable pore size in nanometers are of interest for efficient and energy-saving separation processes.[1–6] Recently, the observation of precise molecular sieving and fast solvent permeation through graphene-oxide membranes (GOMs) has aroused intense interest due to their potential for application in water filtration, molecular separation and desalination.[7–11] The laminar GOMs can be readily obtained through vacuum filtration, spin coating or a layer-by-layer self-assembly approach.[12–15] The selective molecular sieving of laminar GOMs is primarily dependent on the size cut-off effect.[16–18] However, it is difficult to maintain the pores of laminar GOMs—that is the interstitial space between graphene oxide laminates— when immersing laminar GOMs in aqueous solution due to the swelling of interlayer channels (as schematically elucidated in Fig. 1a).[19–21] The mass transport across the laminar GOMs in the vertical direction is usually low because of the intricate transport path and low permeability (Fig. 1a).[22,23] These challenges hinder the potential applications of laminar GOMs in real separation processes.

Two-dimensional covalent organic frameworks (2D COFs) are emerging crystalline porous materials with a precisely controlled pore size, functionalized pore surface and nanochannels in their vertical direction (Fig. 1b).[24–30] Most of the conventional COF synthetic approaches offer poor control of their morphology and result in an insoluble and unprocessable microcrystalline powder.[31–34] Although some COF powders can be transformed into covalent organic nanosheets (CONs) *via* further exfoliation under mechanical grinding, ultra-sonication or chemical processes,[35–42] the resulting CONs lead to tiny size and vast internal structural defects due to the rough operation procedure, which impedes CONs from further assembling into integral and large-scale COF membranes for separation.[43] Recently, Banerjee *et al.* reported the preparation of COF thin films by virtue of the interface crystallization process.[44] This strategy allows simultaneous control over the crystallization and morphology of COF films. However, these COF films still rely on neutral framework structures. Integration of ionic modules into porous membranes would induce novel functions distinct from those of neutral membranes, especially when the

[a]State Key Laboratory of Luminescence and Applications, Changchun Institute of Optics, Fine Mechanics and Physics, Chinese Academy of Sciences, Changchun 130033, P. R. China. E-mail: libinteacher@163.com

[b]University of Chinese Academy of Sciences, Beijing 100049, P. R. China

[c]School of Chemical Engineering and Technology, Xi'an Jiaotong University, Xi'an 710049, China. E-mail: maheping@mail.xjtu.edu.cn

† Electronic supplementary information (ESI) available: Experimental details, materials and reagents, apparatus, conditions and methods. See DOI: 10.1039/c8ta04178d

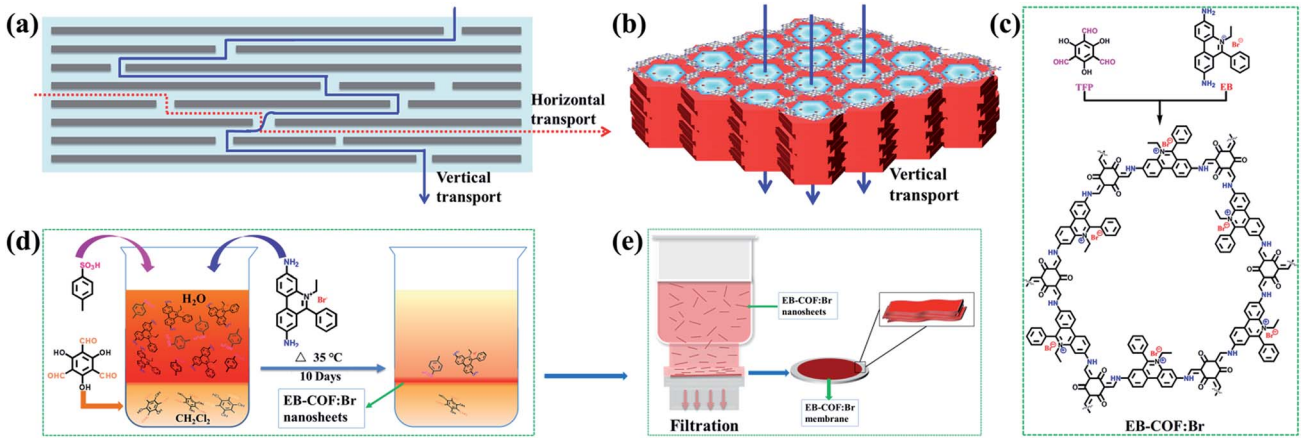

Fig. 1 (a) The model of the lamellar film with massive arrays of 2D graphene oxide (GO) sheets, the mass transfer can be achieved both along the sheets (horizontal transport) and across GO sheets at defects (vertical transport). (b) The mass transport across the COFs membrane along the 1D nanochannels in the vertical direction. (c) Chemical structures and schematic of the synthesis of EB-COF:Br *via* the condensation of EB and TFP at 35 °C. (d) Schematic representation of the interfacial crystallization process used to synthesize the EB-COF:Br nanosheets; the bottom faint-yellow layer corresponds to the aldehyde in dichloromethane solution, and the top orange-red layer is EB amine-PTSA aqueous solution. (e) Schematic representation of the preparation process of the EB-COF:Br membrane *via* layer-by-layer restacking of EB-COF:Br nanosheets.

pore size of the membrane is below 100 nm.[45] In extremely limited space, the remarkable electrostatic interaction is superimposed with confinement of the nanochannels; the mass transport in the charged channel will be double-controlled by the size and charge.[46,47] In this sense, lots of unexpected and exciting phenomena of nanoconfined transports such as highly selective ion permeation and ultrafast solvent permeation are predicted in the charged COF membranes.[48] Accordingly, we prepared a 2D cationic COF membrane with accessible ionic units and uniform nanosize channels for selective molecular sieving.

We introduced a salt-mediated technique to fabricate a cationic COF, EB-COF:Br, as a large-scale membrane by combining a cationic monomer, ethidium bromide (EB) (3,8-diamino-5-ethyl-6-phenylphenanthridinium bromide), with 1,3,5-triformylphloroglucinol (TFP) through a Schiff base reaction at 35 °C (Fig. 1c).[31,44] The highly crystalline porous 2D cationic COF nanosheets were definitely retained at the liquid–liquid interface and were easily transferable to various substrates (Fig. 1d and S1, ESI†).[44] Then a layer-by-layer restacking process was performed to assemble a continuous and dense EB-COF:Br membrane with a tunable thickness by handy vacuum filtration of different amounts of nanosheet dispersion liquid on the nylon 66 support (Fig. 1e).[49,50] The cationic EB-COF:Br membrane exhibited excellent selective sieving for ionic pollutants of different molecular sizes and charges, along with high solvent permeability. To the best of our knowledge, this is the first positively charged 2D COF membrane with excellent selective sieving performance.

Results and discussion

The interfacial crystallization approach was used to synthesize stable keto-enol tautomerism-based EB-COF:Br nanosheets by a Schiff base reaction (Fig. 1c).[44,51–53] The Fourier transform infrared (FT-IR) spectra of the initial monomers and EB-COF:Br had been measured and are shown in Fig. S2a (ESI†). The aldehyde group stretching bands of TFP (-C=O at 1642 cm^{-1}, O=C–H at 2890 cm^{-1}) and the N–H stretching bands of EB disappeared (3196 cm^{-1}, 3303 cm^{-1}), which provides direct evidence for the completion of the co–condensation reaction. Meanwhile, the lack of –OH and imine (C=N) stretching bands and the rise of the C=C stretching peak at 1594 cm^{-1} (Fig. S2b, ESI†) show that EB-COF:Br exists in the keto form.[54] One of the advantages of interfacial crystallization is that we can transfer the film onto different substrates. Fig. 2a is the digital image of a large-scale film that we transferred onto porous glass. We further use atomic force microscopy (AFM), transmission electron microscopy (TEM) and scanning electron microscopy (SEM) to gain insight into the internal structure of the COF nanosheets and membrane. AFM was used to estimate the thickness of the EB-COF:Br nanosheets. The nanosheets were dispersed into ethanol by sonication and then drop-cast on a silicon wafer for AFM measurements. AFM analysis results indicate that the heights of EB-COF:Br nanosheets are in the range of ~155–165 nm (Fig. 2d and e). These nanosheets were then loaded on a carbon-coated copper grid for TEM analysis. As shown in Fig. 2g, the TEM image of EB-COF:Br nanosheets reveals a high degree of crystallinity, as demonstrated by the clear lattice fringes. Ordered straight channels with a spacing of 1.65 nm were observed. The 1.65 nm channel is close to the pore size of the simulated EB-COF:Br structure (1.7 nm). After a restacking process, the nanosheets can be assembled into an integrated membrane. The SEM images reveal that the EB-COF:Br membrane is continuous and free of defects on the surface (Fig. 2b), which is critical for efficient separation. The cross-sectional SEM view of the EB-COF:Br membrane shows a stacked structure similar to that of laminar GOMs (Fig. 2c).[14,55]

X-ray diffraction (XRD) was performed to confirm the structure of the EB-COF:Br membrane. The XRD spectrum of the

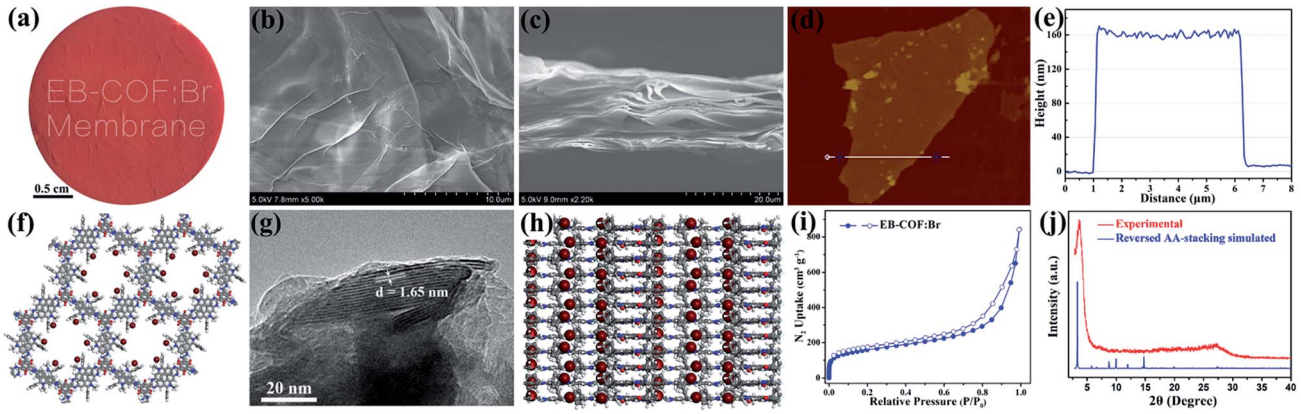

Fig. 2 Characterization of the EB-COF:Br nanosheets and EB-COF:Br membrane: (a) photograph of the EB-COF:Br membrane; (b) surface SEM image of the EB-COF:Br membrane; (c) cross-sectional SEM image of the EB-COF:Br membrane; (d) and (e) AFM images of the EB-COF:Br nanosheets showing the surface roughness and thickness recorded on the top of a silicon wafer, respectively; (f) schematic monolayer extended structure of EB-COF:Br; (g) TEM image of the of EB-COF:Br nanosheets; (h) side view of the reversed slipped AA-stacking model structure of EB-COF:Br; (i) nitrogen sorption isotherm for EB-COF:Br; (j) XRD pattern of EB-COF:Br.

membrane shows two main peaks which were assigned to the 100 and 001 planes, respectively. As shown in Fig. 2j, the observed XRD pattern matches well with the simulated XRD pattern of the reversed slipped AA-stacking model.[56] We can see clearly that the first peak in the XRD corresponds to the 100 plane which appears at 3.3 Å. And the peak at 27° in the XRD pattern is assigned to the 001 plane that corresponds to the π–π stacking of EB-COF:Br layers. We notice that the peak at 27° is broad and blunt, which is due to the reversed slipped AA-stacking model and the defects in the π–π stacking between successive 2D COF layers.[40,56] Subsequently, structural resolution based on the X-ray diffraction pattern in conjunction with the simulated structure indicates that the as-synthesized EB-COF:Br is a typical 2D layered hexagonal network (Fig. 2f and h and S3, ESI†).[56]

In order to investigate the porosity and pore size of the EB-COF:Br membrane, the nitrogen adsorption–desorption experiment of the membrane was performed at 77 K. As shown in Fig. 2i, a sharp increase was observed in the gas uptake at low pressure, which means that these are micropores in the membrane. The surface area calculated on the basis of the Brunauer–Emmett–Teller (BET) model is 554 $m^2\ g^{-1}$ for EB-COF:Br. We also observe the hysteresis curve in desorption, which may be caused by the stack of EB-COF:Br nanosheets. Because it is very difficult to ensure that every piece of nanosheet is completely tiled during the process of layer-by-layer restacking, a fraction of nanosheets may be folded or crimped, which will result in interstices between the nanosheets within the membrane (shown in Fig. 2c). The pore size distribution of the EB-COF:Br membrane was evaluated by the nonlocal density functional theory method based on the model N_2 at 77 K on carbon. EB-COF:Br mainly exhibits a pore size of 16.8 Å (Fig. S4, ESI†). The above results support that the EB-COF:Br membrane is a porous 2D crystallized COF membrane with uniform 1D channels.

Considering that the EB-COF:Br membrane has nanosize channels and positive charges on pore walls, it can be utilized for selective sieving for molecules/ions. Initially, the molecular weight cut-off (MWCO) analysis was performed from the rejection of polyethylene glycol (PEG) with different average molecular weights (200, 400, 600, 800, 1000 and 1500 Da). The results show that the EB-COF:Br membrane has 90% rejection of PEG at 882 Da (Fig. 3a). According to the results of MWCO analysis, we can conclude that the porosity of the EB-COF:Br membrane is within the nanofiltration range. Furthermore, we investigated the permeability of the EB-COF:Br membrane to a pure solvent. Exhilaratingly, the EB-COF:Br membrane exhibits excellent permeance towards protic solvents, including deionized water (546 L $m^{-2}\ h^{-1}\ bar^{-1}$), methanol (1272 L $m^{-2}\ h^{-1}\ bar^{-1}$), ethanol (564 L $m^{-2}\ h^{-1}\ bar^{-1}$), n-propanol (477 L $m^{-2}\ h^{-1}\ bar^{-1}$), n-butanol (378 L $m^{-2}\ h^{-1}\ bar^{-1}$), *n*-pentanol (248 L $m^{-2}\ h^{-1}\ bar^{-1}$) and *n*-hexanol (166 L $m^{-2}\ h^{-1}\ bar^{-1}$). Meanwhile, the permeability is decreased along with increasing molecular size of the permeant solvents (Fig. 3b and Table S1, ESI†). To our surprise, the membrane shows higher permeance towards organic aprotic solvents, such as acetone (2640 L $m^{-2}\ h^{-1}\ bar^{-1}$), followed by acetonitrile (2095 L $m^{-2}\ h^{-1}\ bar^{-1}$), tetrahydrofuran (1532 L $m^{-2}\ h^{-1}\ bar^{-1}$), 1,4-dioxane (973 L $m^{-2}\ h^{-1}\ bar^{-1}$) and *N*,*N*′-dimethylacetamide (565 L $m^{-2}\ h^{-1}\ bar^{-1}$) (Fig. 3c and Table S2, ESI†). The high permeance of the organic aprotic solvents can be attributed to the weak dipole interaction between these aprotic solvents and the charged interface aligned in the channel in the EB-COF:Br membrane. It is worth mentioning that the solvent permeability of the EB-COF:Br membrane is much higher than those of GOMs and other reported nanofiltration membranes (See Table S3, ESI† for detailed comparisons).[8,19,57–59] Furthermore, we also evaluate the impact of the membrane thickness on the permeability of the pure solvent. The filtration experiment for deionized water is conducted using several membranes with different thicknesses (146 μm, 195 μm, 241 μm, respectively). As shown in Fig. 3b inset and Table S4 (ESI†), the permeance value of deionized water decreases as the membrane thickness increases in turn.

Graphene-oxide membranes (GOMs) with interlayer space between GO flakes have been reported to be potentially applied

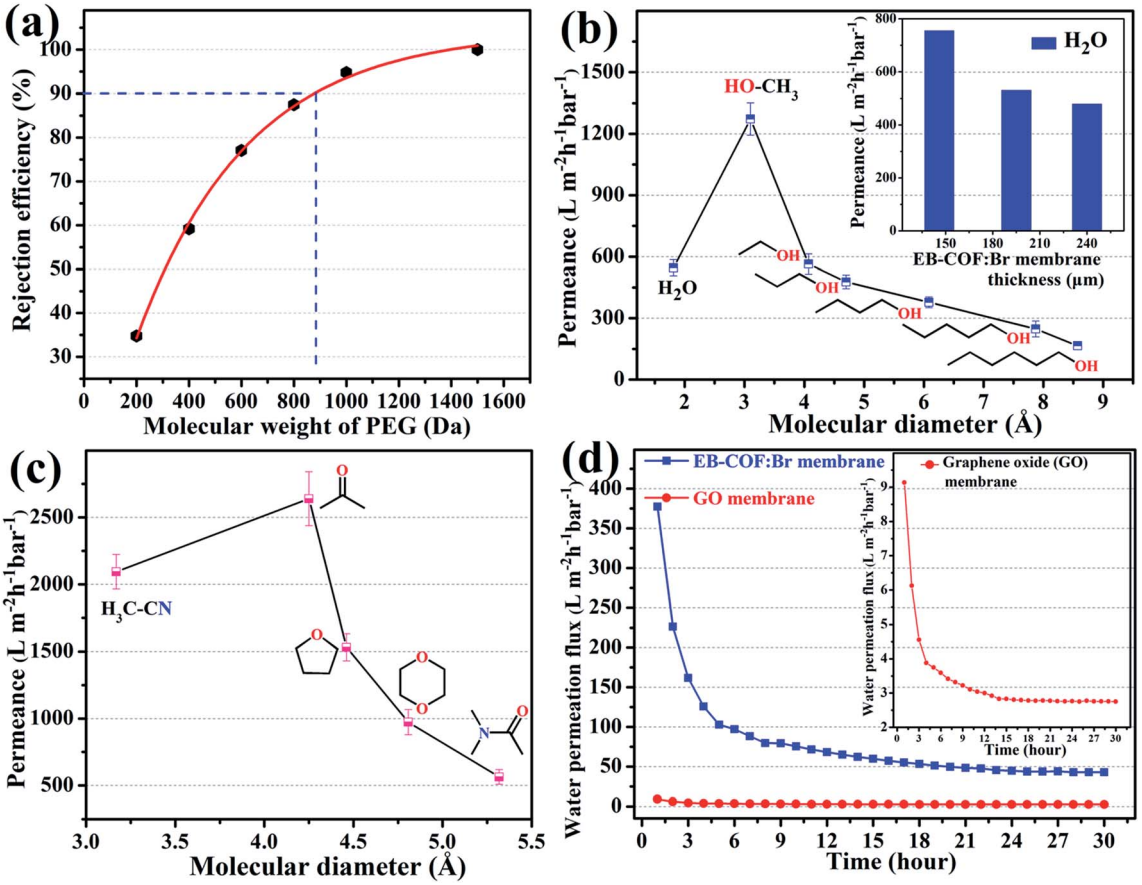

Fig. 3 (a) Molecular-weight cut-off (MWCO) curve showing that the EB-COF:Br membrane has 90% rejection of PEG at 882 Da; (b) pure solvent permeance *versus* molecular diameter of different protic (water, methanol, ethanol, n-propanol, n-butanol, 1-pentanol, and n-hexyl alcohol) and (c) aprotic (acetonitrile, acetone, tetrahydrofuran, 1,4-dioxane, and *N*,*N*-dimethylacetamide) solvents; (d) water permeation flux of the EB-COF:Br membrane and GO membrane as a function of time. The membranes were prepared using filtration with a thickness of about 308 μm for the EB-COF:Br membrane and 3.6 μm for the GO membrane.

in the separation and desalination of small molecules. However, severe reduction of water permeability was observed in GOMs in the pressure-driven permeation test due to the compaction of their loosely packed microstructure. The water flux could drop continuously after more than ten hours as a result of the efficient transport channel reduction over time.[60,61] One advantage of 2D COF membranes is that they have a straight channel along with the solvent transport path (Fig. 1b). We make a comparison of water permeation performance between the EB-COF:Br membrane and GOMs. As shown in Fig. 3d and S5 and S6 (ESI†), the water permeability of GOMs is 2.5 L m^{-2} h^{-1} bar^{-1} after the 30 hour test (Fig. 3d inset, S5, ESI†). Although the water permeability of the EB-COF:Br membrane is also drastically reduced in the beginning of the permeation test, the steady state water flux of the EB-COF:Br membrane is 48 L m^{-2} h^{-1} bar^{-1} after 30 hours of continuous testing (Fig. S6, ESI†). This water flux is about 20 times higher than the permeability of GOMs.

The significant advantages of high flux and outstanding chemical stability of the EB-COF:Br membrane motivate us to further investigate the rejection performance toward a series of pollutants with environmental and industrial concerns. We choose several water-soluble target dye molecules/ions with different properties of charge, including anionic dyes: Methyl Orange (MO), Fluorescein Sodium salt (FSs) and Potassium Permanganate (PP); neutral dyes: Nile Red (NR), Calcein (CA) and *p*-Nitroaniline (NA) and cationic dyes: Rhodamine B (RB), Methylene Blue (MB) and *N*,*N*-dimethyl-*p*-phenylenediamine dihydrochloride (DMPD). Most of these dyes are mutagenic and carcinogenic in nature, which can cause serious health problems. The sizes of these molecules are assumed by a long-axis dimension of an ellipsoid, as shown in Fig. S7 (ESI†). Their corresponding chemical structures and properties are shown in Fig. 4 and Table S5 (ESI†).

We conducted a series of filtration experiments with solutions of dye molecules and ions through the EB-COF:Br membrane to verify its rejection performance. The rejection ability of the membrane toward different target dyes was evaluated by monitoring the ultraviolet absorbance intensity of filtrates. As shown in Fig. 5, for anionic dyes (MO, FS and PP), the intensity of absorption spectra of different anionic dyes displays a sharp decrease, as observed in Fig. 5a–c. The characteristics absorption bands of MO, FSs and PP completely disappeared after filtration through the EB-COF:Br membrane.

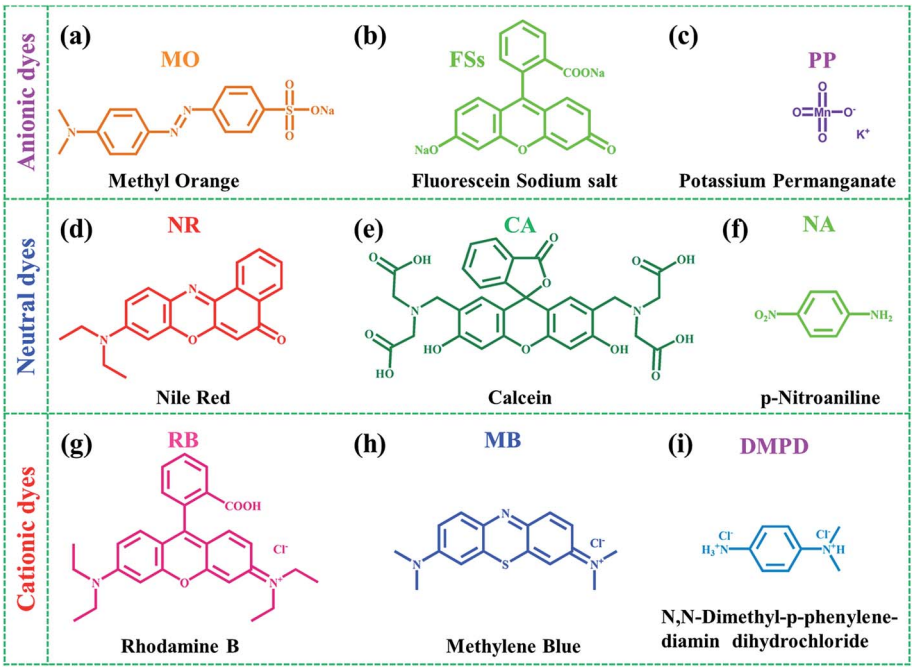

Fig. 4 Chemical structures of dye molecules/ions. (a) MO (methyl orange); (b) FSs (fluorescein sodium salt); (c) PP (potassium permanganate); (d) NR (nile red); (e) CA (calcein); (f) NA (*p*-nitroaniline); (g) RB (rhodamine B); (h) MB (methylene blue) and (i) DMPD (*N*,*N*-dimethyl-*p*-phenylenediamine dihydrochloride).

The three neutral dyes present a smaller decline in the intensity of characteristic absorption spectra, especially for NR and NA (Fig. 5d–f). For cationic dyes (RB, MB and DMPD), the characteristic absorption intensity of these dyes is also decreased very significantly (Fig. 5g–i); however, the decreasing amplitude is less than that of the anionic dyes. A more intuitive piece of evidence of the highly selective sieving performance of the EB-COF:Br membrane is also shown in theFig. 5l; we can observe clearly the color change of different dye solutions before sieving and after sieving *via* the naked eye under visible light. Remarkably, for anionic dyes, several colorless filtrates are obtained after the EB-COF:Br membrane filtration (Fig. 5j(a–c)). However, other filtrates, from neutral dyes (NR, CA, and NA) (Fig. 5k(d–f)) and cationic dyes (RB, MB, and DMPD) (Fig. 5l(g–i)) solutions, still retain their partial color, which indicates that some dye molecules/ions have permeated the membrane.

In order to more accurately determine the rejection efficiency of the EB-COF:Br membrane for different target dyes a qualitative calculation in terms of the Beer–Lambert law is performed. The result shows that the membrane can reject anionic dyes MO, FSs and PP up to 99.6%, 99.2% and 98.1%, respectively. The rejection values of cationic dyes RB, MB and DMPD are 91.2%, 87.2% and 84.9%, respectively. Whereas for neutral dyes of CA, NR and NA, the rejection values are 74.4%, 22.3% and 15.7%, respectively (Fig. 6). The interception efficiency of this 2D cationic membrane for neutral dyes has positive correlation with the molecular size. The rejection efficiency of the EB-COF:Br membrane for charged dyes can compete with those of other high performance membranes. (Table S6, ESI†).

The above experimental results confirm that the EB-COF:Br membrane has excellent selective sieving performance for different dye molecules/ions, which is mainly attributed to the following reasons: primarily, plenty of positively charged sites are distributed on the pore walls of the EB-COF:Br membrane, which endows the membrane with a cationic nature. Moreover, EB-COF:Br has a reversed slipped AA-stacking structure with 16.8 Å pore size. Such spatial alignment vastly enhances the accessibility of cationic sites for guest molecules/ions. Additionally, molecular rejection for the COF membrane not only involves charge-driven separation, but also includes a physical size sieving effect. Based on the structural properties of the EB-COF:Br membrane, its selective molecular/ionic sieving performance can be explained as follows.

For anionic dye sieving: in the beginning, the negatively charged molecules can replace the counter-ions Br^{1-} to fit in the channels. Owing to the strong electrostatic interaction between the positively charged pore walls of the membrane and anionic dye molecules,[46] the dye molecules will be immobilized into the pores of the membrane, preventing them from being moved down along the channels. Moreover, duo to the size limitation of nanoscale channels, only one dye molecule enters the EB-COF:Br channel each time. So the subsequent molecule cannot cross the membrane. Although the channels of the EB-COF:Br membrane are blocked by early entered dye molecules, there's still enough space for solvent molecules to pass through the membrane. So the excellent anionic molecule rejection of the membrane is double-controlled by the electrostatic interaction and the limitation of the pore size.

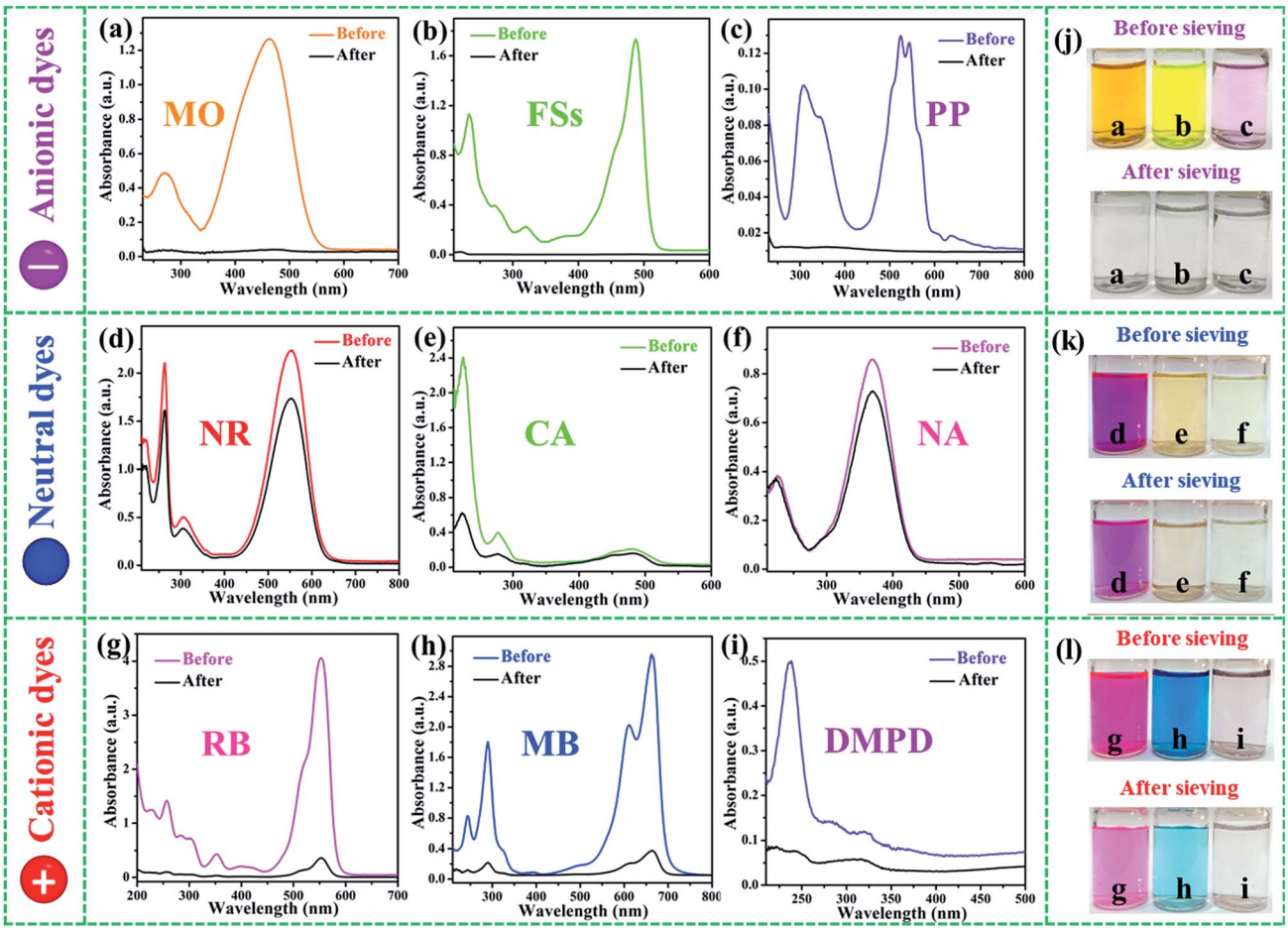

Fig. 5 Charge- and size-selective sieving experiments. (a–i) UV-vis absorption spectra of different dye solutions of (a) MO (methyl orange), (b) FSs (fluorescein sodium salt), (c) PP (potassium permanganate), (d) NR (nile red), (e) CA (calcein), (f) NA (*p*-nitroaniline), (g) RB (rhodamine B), (h) MB (methylene blue) and (i) DMPD (*N*,*N*-dimethyl-*p*-phenylenediamine dihydrochloride) before sieving and after sieving through the EB-COF:Br membrane, respectively. Photographs of the color change of different dye solutions before and after sieving are shown in (j), (k), (l), respectively.

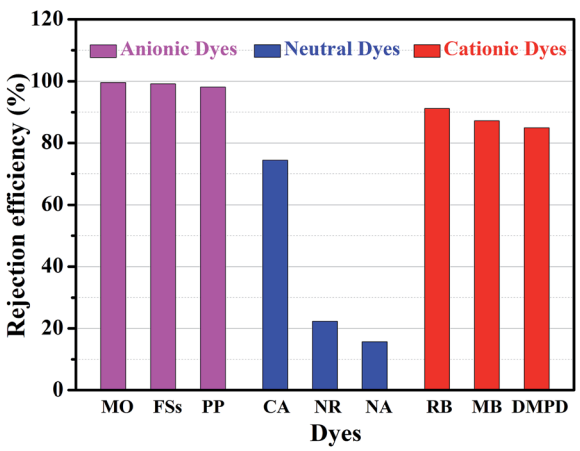

Fig. 6 The rejection efficiency of the EB-COF:Br membrane for different dyes.

In comparison, the rejection values of cationic dyes are lower than those of anionic dyes. Because of the strong electrostatic repulsion interaction between the positively charged pore surface and cationic dye molecules, it will hinder the molecules entering into the pore channels of the EB-COF:Br membrane. In spite of this, small cationic dye molecules such as DMPD will still be able to diffuse into the channels slowly. Due to the repulsive force in the positively charged pore, the cationic dye molecules cannot be fixed in the channels and they will cross the membrane. So the discrepancy of separation efficiency between cationic dye molecules mainly originates from their molecular sizes (Fig. S7g–i, ESI†).

As for neutral dye molecules, the electrostatic interaction between the dye and EB-COF:Br is very weak. Hence, the rejection efficiency is mainly attributed to the molecular size sieving effect. As shown in Fig. 6, the rejection values for the neutral dye are in good agreement with their molecular size: NA < NR < CA (Fig. 5d–f, 6 and S7d–f, ESI†).

To evaluate the mixed dye solution separation ability of the membrane, a mixed solution of FSs (Fluorescein Sodium salt) and NA (nitroaniline) is filtered *via* the EB-COF:Br membrane. As shown in Fig. 7, a greenish yellow mixed solution [derived from yellow (FSs) and reseda (NA)] is filtered through the EB-COF:Br membrane, resulting in a light yellow NA filtrate (Fig. 7a). This result is further confirmed by comparing the UV-

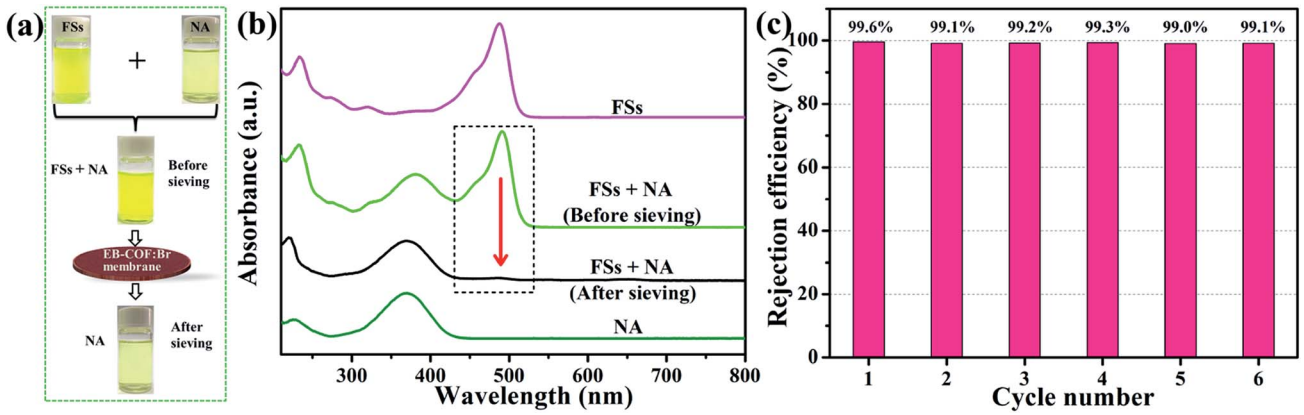

Fig. 7 (a) Photograph schematic of the selective molecular separation of nitroaniline (NA) from a mixture of NA and Fluorescein Sodium salt (FSs); (b) UV-vis absorption spectra of selective sieving of NA from the mixed solution of NA and FSs; (c) cycle performance of MO rejection through the EB-COF:Br membrane.

vis absorption spectra of the mixed solution before and after separation, respectively. The concentration of FSs in the filtrate is decreased by 98%, whereas NA does not show any notable changes (Fig. 7b), which consequently confirms that FSs and NA can be effectively separated. In addition, another mixed dye solution (including anionic, neutral and cationic dyes) had also been filtered *via* the EB-COF:Br membrane. As shown in Fig. S8 and S9 (ESI†), the absorbance spectrum of the solution before- and after-filtration further demonstrated that the EB-COF:Br membrane could thoroughly intercept the anionic dye molecules, manifesting its potential application towards complex wastewater treatment in textile/dye industries.

As a promising separation membrane, the recyclability is very important. Here, a cycling study of the EB-COF:Br membrane for MO interception is carried out. The result demonstrates that the cationic nanochannels of the EB-COF:Br membrane can be easily rinsed thoroughly and regenerated by treating the membrane with aqueous NaBr solution (2.0 mol L^{-1}). As shown in Fig. 7c and Fig. S10 (ESI†), the rejection efficiency of the recycled EB-COF:Br membrane for MO is above 99.1% even after six cycles. Furthermore, the time course of rejection efficiency of the EB-COF:Br membrane for the anionic dye (MO) was also performed to investigate the durability of the membrane. As can be seen in Fig. S11 (ESI†), the membrane still exhibits >99% rejection efficiency for MO after 10 hours of continuous operation. All the above results indicate that the cationic COF membrane combines selectivity, efficiency and recyclability in rejection of anionic dyes, manifesting its potential in application towards wastewater treatment in textile/dye industries and environmental protection.

Conclusions

In summary, a 2D cationic crystallized COF membrane, namely EB-COF:Br membrane, was fabricated by a facile bottom-up interfacial crystallization approach and layer-by-layer restacking process. We demonstrated that the 2D EB-COF:Br offered an excellent scaffold for creating ionic interfaces in pore walls along the channels in the membrane. The resulting EB-COF:Br membrane exhibited remarkable selective molecular sieving performance based on their different sizes and charges. Given the unique structure of the EB-COF:Br membrane, physical size sieving and electrostatic interactions are considered to play a vital role in the process of separation. The reported cationic 2D COFs membrane exhibits extraordinary separation properties with high solvent permeability. With the ultrafast solvent transport and selective molecular sieving properties, the ionic COF membrane can be presented as an interesting platform for separation and filtration technologies.

Conflicts of interest

The authors declare no competing financial interests.

Acknowledgements

The authors gratefully acknowledge the financial support of the NSFC (Grant No. 21773223, 21673218, 51572256, 21501166) and the Science and Technology Developing Project of Jilin Province (Grant No. 20170520135JH, 20180101177JC, 20180101176JC). The authors also thank the Open Funds of the State Key Laboratory of Rare Earth Resource Utilization and State Key Laboratory of Inorganic Synthesis and Preparative Chemistry, Jilin University.

Notes and references

1 J. W. Colson and W. R. Dichtel, *Nat. Chem.*, 2013, **5**, 453–465.
2 Y. Ying, Y. Yang, W. Ying and X. Peng, *Nanotechnology*, 2016, **27**, 332001.
3 L. S. Wan, J. W. Li, B. B. Ke and Z. K. Xu, *J. Am. Chem. Soc.*, 2012, **134**, 95–98.
4 P. Sun, K. Wang and H. Zhu, *Adv. Mater.*, 2016, **28**, 2287–2310.

5 Q. Wen, D. Yan, F. Liu, M. Wang, Y. Ling, P. Wang, P. Kluth, D. Schauries, C. Trautmann, P. Apel, W. Guo, G. Xiao, J. Liu, J. Xue and Y. Wang, *Adv. Funct. Mater.*, 2016, **26**, 5796–5803.
6 A. Lee, J. W. Elam and S. B. Darling, *Environ. Sci.: Water Res. Technol.*, 2016, **2**, 17–42.
7 R. K. Joshi, P. Carbone, F. C. Wang, V. G. Kravets, Y. Su, I. V. Grigorieva, H. A. Wu, A. K. Geim and R. R. Nair, *Science*, 2014, **343**, 752–754.
8 Q. Yang, Y. Su, C. Chi, C. T. Cherian, K. Huang, V. G. Kravets, F. C. Wang, J. C. Zhang, A. Pratt, A. N. Grigorenko, F. Guinea, A. K. Geim and R. R. Nair, *Nat. Mater.*, 2017, **16**, 1198–1202.
9 H. M. Hegab and L. Zou, *J. Membr. Sci.*, 2015, **484**, 95–106.
10 J. R. Werber, C. O. Osuji and M. Elimelech, *Nat. Rev. Mater.*, 2016, **1**, 16018.
11 D. Cohen-Tanugi and J. C. Grossman, *Nano Lett.*, 2012, **12**, 3602–3608.
12 F. X. Xiao, M. Pagliaro, Y. J. Xu and B. Liu, *Chem. Soc. Rev.*, 2016, **45**, 3088–3121.
13 H. Huang, Z. Song, N. Wei, L. Shi, Y. Mao, Y. Ying, L. Sun, Z. Xu and X. Peng, *Nat. Commun.*, 2013, **4**, 2979.
14 K. Raidongia and J. Huang, *J. Am. Chem. Soc.*, 2012, **134**, 16528–16531.
15 H. Li, Z. Song, X. Zhang, Y. Huang, S. Li, Y. Mao, H. J. Ploehn, Y. Bao and M. Yu, *Science*, 2013, **342**, 95–98.
16 P. R. Kidambi, M. S. H. Boutilier, L. Wang, D. Jang, J. Kim and R. Karnik, *Adv. Mater.*, 2017, **29**, 1605896.
17 G. Liu, W. Jin and N. Xu, *Chem. Soc. Rev.*, 2015, **44**, 5016–5030.
18 K. Celebi, J. Buchheim, R. M. Wyss, A. Droudian, P. Gasser, I. Shorubalko, J. I. Kye, C. Lee and H. G. Park, *Science*, 2014, **344**, 289–292.
19 Y. Han, Z. Xu and C. Gao, *Adv. Funct. Mater.*, 2013, **23**, 3693–3700.
20 C. Cheng, G. Jiang, C. J. Garvey, Y. Wang, G. P. Simon, J. Z. Liu and D. Li, *Sci. Adv.*, 2016, **2**, 1501272.
21 L. Chen, G. Shi, J. Shen, B. Peng, B. Zhang, Y. Wang, F. Bian, J. Wang, D. Li, Z. Qian, G. Xu, G. Liu, J. Zeng, L. Zhang, Y. Yang, G. Zhou, M. Wu, W. Jin, J. Li and H. Fang, *Nature*, 2017, **550**, 380–383.
22 A. R. Koltonow and J. Huang, *Science*, 2016, **351**, 1395–1396.
23 S. Wang, Y. Xie, G. He, Q. Xin, J. Zhang, L. Yang, Y. Li, H. Wu, Y. Zhang, M. D. Guiver and Z. Jiang, *Angew. Chem., Int. Ed.*, 2017, **56**, 14246–14251.
24 U. Díaz and A. Corma, *Coord. Chem. Rev.*, 2016, **311**, 85–124.
25 R. P. Bisbey and W. R. Dichtel, *ACS Cent. Sci.*, 2017, **3**, 533–543.
26 C. S. Diercks and O. M. Yaghi, *Science*, 2017, **355**, 923–931.
27 X. Zhuang, Y. Mai, D. Wu, F. Zhang and X. Feng, *Adv. Mater.*, 2015, **27**, 403–427.
28 N. Huang, X. Chen, R. Krishna and D. Jiang, *Angew. Chem., Int. Ed.*, 2015, **54**, 2986–2990.
29 J. L. Segura, M. J. Mancheno and F. Zamora, *Chem. Soc. Rev.*, 2016, **45**, 5635–5671.
30 P. J. Waller, F. Gandara and O. M. Yaghi, *Acc. Chem. Res.*, 2015, **48**, 3053–3063.
31 S. Kandambeth, B. P. Biswal, H. D. Chaudhari, K. C. Rout, H. S. Kunjattu, S. Mitra, S. Karak, A. Das, R. Mukherjee, U. K. Kharul and R. Banerjee, *Adv. Mater.*, 2017, **29**, 1603945.
32 S. Y. Ding and W. Wang, *Chem. Soc. Rev.*, 2013, **42**, 548–568.
33 S. Kandambeth, A. Mallick, B. Lukose, M. V. Mane, T. Heine and R. Banerjee, *J. Am. Chem. Soc.*, 2012, **134**, 19524–19527.
34 J. W. Colson, A. R. Woll, A. Mukherjee, M. P. Levendorf, E. L. Spitler, V. B. Shields, M. G. Spencer, J. Park and W. R. Dichtel, *Science*, 2011, **332**, 228–231.
35 S. Chandra, S. Kandambeth, B. P. Biswal, B. Lukose, S. M. Kunjir, M. Chaudhary, R. Babarao, T. Heine and R. Banerjee, *J. Am. Chem. Soc.*, 2013, **135**, 17853–17861.
36 J. Zhang, Y. Chen and X. Wang, *Energy Environ. Sci.*, 2015, **8**, 3092–3108.
37 D. N. Bunck and W. R. Dichtel, *J. Am. Chem. Soc.*, 2013, **135**, 14952–14955.
38 S. Wang, Q. Wang, P. Shao, Y. Han, X. Gao, L. Ma, S. Yuan, X. Ma, J. Zhou, X. Feng and B. Wang, *J. Am. Chem. Soc.*, 2017, **139**, 4258–4261.
39 G. Das, B. P. Biswal, S. Kandambeth, V. Venkatesh, G. Kaur, M. Addicoat, T. Heine, S. Verma and R. Banerjee, *Chem. Sci.*, 2015, **6**, 3931–3939.
40 Z. Kang, Y. Peng, Y. Qian, D. Yuan, M. A. Addicoat, T. Heine, Z. Hu, L. Tee, Z. Guo and D. Zhao, *Chem. Mater.*, 2016, **28**, 1277–1285.
41 S. Mitra, S. Kandambeth, B. P. Biswal, M. A. Khayum, C. K. Choudhury, M. Mehta, G. Kaur, S. Banerjee, A. Prabhune, S. Verma, S. Roy, U. K. Kharul and R. Banerjee, *J. Am. Chem. Soc.*, 2016, **138**, 2823–2828.
42 M. A. Khayum, S. Kandambeth, S. Mitra, S. B. Nair, A. Das, S. S. Nagane, R. Mukherjee and R. Banerjee, *Angew. Chem., Int. Ed.*, 2016, **55**, 15604–15608.
43 X. H. Liu, C. Z. Guan, D. Wang and L. J. Wan, *Adv. Mater.*, 2014, **26**, 6912–6920.
44 K. Dey, M. Pal, K. C. Rout, H. S. Kunjattu, A. Das, R. Mukherjee, U. K. Kharul and R. Banerjee, *J. Am. Chem. Soc.*, 2017, **139**, 13083–13091.
45 D. Xu, J. Guo and F. Yan, *Prog. Polym. Sci.*, 2018, **79**, 121–143.
46 N. Huang, P. Wang, M. A. Addicoat, T. Heine and D. Jiang, *Angew. Chem., Int. Ed.*, 2017, **56**, 4982–4986.
47 C. Yan, C. Lv, Y. Zhu, G. Chen, J. Sun and G. Yu, *Adv. Mater.*, 2017, **29**, 1703909.
48 X. Lin, Q. Yang, L. Ding and B. Su, *ACS Nano*, 2015, **9**, 11266–11277.
49 Y. Ying, D. Liu, J. Ma, M. Tong, W. Zhang, H. Huang, Q. Yang and C. Zhong, *J. Mater. Chem. A*, 2016, **4**, 13444–13449.
50 J. J. Shao, K. Raidongia, A. R. Koltonow and J. Huang, *Nat. Commun.*, 2015, **6**, 7602.
51 R. Sakamoto, K. Hoshiko, Q. Liu, T. Yagi, T. Nagayama, S. Kusaka, M. Tsuchiya, Y. Kitagawa, W. Y. Wong and H. Nishihara, *Nat. Commun.*, 2015, **6**, 6713.
52 W. Dai, F. Shao, J. Szczerbinski, R. McCaffrey, R. Zenobi, Y. Jin, A. D. Schluter and W. Zhang, *Angew. Chem., Int. Ed.*, 2016, **55**, 213–217.
53 R. Dong, M. Pfeffermann, H. Liang, Z. Zheng, X. Zhu, J. Zhang and X. Feng, *Angew. Chem., Int. Ed.*, 2015, **54**, 12058–12063.

54 B. P. Biswal, S. Chandra, S. Kandambeth, B. Lukose, T. Heine and R. Banerjee, *J. Am. Chem. Soc.*, 2013, **135**, 5328–5331.
55 R. R. Nair, H. A. Wu, P. N. Jayaram, I. V. Grigorieva and A. K. Geim, *Science*, 2012, **335**, 442.
56 H. Ma, B. Liu, B. Li, L. Zhang, Y. G. Li, H. Q. Tan, H. Y. Zang and G. Zhu, *J. Am. Chem. Soc.*, 2016, **138**, 5897–5903.
57 S. Y. Yang, I. Ryu, H. Y. Kim, J. K. Kim, S. K. Jang and T. P. Russell, *Adv. Mater.*, 2006, **18**, 709–712.
58 J. E. Gu, S. Lee, C. M. Stafford, J. S. Lee, W. Choi, B. Y. Kim, K. Y. Baek, E. P. Chan, J. Y. Chung, J. Bang and J. H. Lee, *Adv. Mater.*, 2013, **25**, 4778–4782.
59 S. Karan, Z. Jiang and A. G. Livingston, *Science*, 2015, **348**, 1347–1351.
60 J. Y. Chong, B. Wang and K. Li, *Chem. Commun.*, 2018, **54**, 2554–2557.
61 J. Y. Chong, B. Wang, C. Mattevi and K. Li, *J. Membr. Sci.*, 2018, **549**, 385–392.